Plasmon-Enhanced Photocatalytic Overall Water-Splitting over Au Nanoparticle-Decorated $CaNb_2O_6$ Electrospun Nanofibers

Jiaming Zhang, Xiaoyi Jiang, Jindou Huang, Wei Lu, Zhenyi Zhang*

Key Laboratory of New Energy and Rare Earth Resource Utilization of State Ethnic Affairs Commission; Key Laboratory of Photosensitive Materials and Devices of Liaoning Province, School of Physics and Materials Engineering, Dalian Minzu University, 18 Liaohe West Road, Dalian 116600, P. R. China.
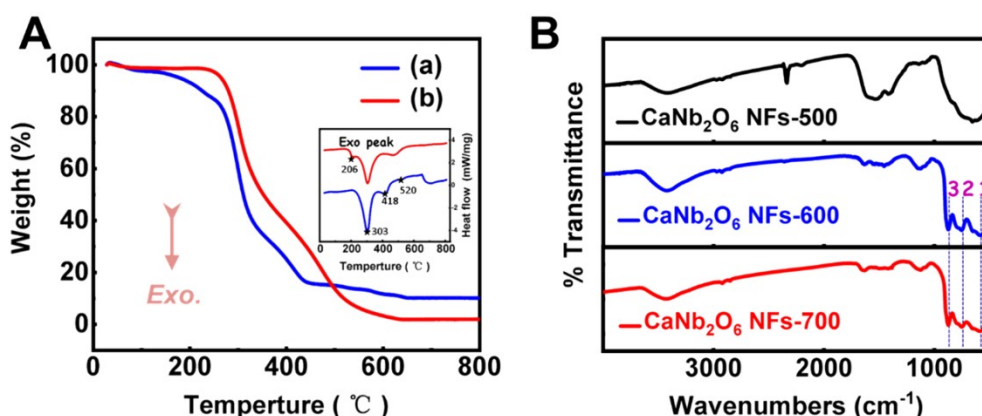
E-mail: zhangzy@dlnu.edu.cn

Fig. S1. (A) TG curves of (a) $PVP/C_{10}H_{14}CaO_4/C_{10}H_5NbO_{20}$ precursor NFs and (b) pure PVP NFs; the inset shows the corresponding DSC curves; (B) FT-IR spectra of $CaNb_2O_6$-500 NFs, $CaNb_2O_6$-600 NFs, and $CaNb_2O_6$-700 NFs.

To investigate the thermal decomposition process of the PVP template, the thermogravimetry (TG) and differential scanning calorimeter (DSC) curves of the $PVP/C_{10}H_{14}CaO_4/C_{10}H_5NbO_{20}$ precursor NFs were measured in comparison with those of the pure PVP NFs (Fig. S1A). For the TG curve of the pure PVP NFs, the first stage of weight loss below 107 °C is mainly ascribed to the loss of residual solvent in the NFs. The pronounced weight loss at the temperature interval between 230 and 380 °C can be attributed to the decomposition of PVP side chains, while the weight loss after 380 °C is mainly ascribed to the decomposition of PVP main chains. After about 600 °C, there was no change in weight loss, suggesting the complete decomposition of PVP. In contrast, the TG curve of the $PVP/C_{10}H_{14}CaO_4/C_{10}H_5NbO_{20}$ NFs presents about 15% weight loss below 245 °C, which

can be attributed to the removal of the residual solvent and the small organic groups of metal salts ($C_{10}H_{14}CaO_4$, and $C_{10}H_5NbO_{20}$) in the NFs. Meanwhile, the dramatic weight loss at the temperature interval between 245 and 440 °C can be assigned to the decomposition of PVP side chains and the oxidation of metal salts. The weight loss originated from the decomposition of PVP main chains started at 440 °C. After about 600 °C, the weight loss was almost kept at ~90 %, indicating the formation of the inorganic oxide. In the case of DSC curve, the pure PVP NFs shows three exothermic peaks at 206, 303 and 520 °C, which can be attributed to the decompositions of the side and main chains of PVP. After introducing the metal salts ($C_{10}H_{14}CaO_4$, and $C_{10}H_5NbO_{20}$) into PVP NFs, the exothermic peak at 203 °C disappeared on the DSC curve of the $PVP/C_{10}H_{14}CaO_4/C_{10}H_5NbO_{20}$ NFs. Meanwhile, a new exothermic peak at 418 °C can be detected, which suggests the existence of interaction between the metal ions and the active groups of PVP in the $PVP/C_{10}H_{14}CaO_4/C_{10}H_5NbO_{20}$ NFs. The above results indicate that the organic components in the $PVP/C_{10}H_{14}CaO_4/C_{10}H_5NbO_{20}$ NFs can be removed at the calcination temperature above 600°C. Thus, in our manuscript, we deduced that the lack of feature diffraction peaks of $CaNb_2O_6$ crystal on the XRD pattern of $CaNb_2O_6$-500 NFs was ascribed to the residual carbon-based compounds and the small grain-sizes of $CaNb_2O_6$ crystal with a poor crystallinity.[1-3]

In order to further confirm the above assumption, the Fourier transform infrared spectroscopy (FT-IR) measurement was carried out on the $CaNb_2O_6$-500 NFs, $CaNb_2O_6$-600 NFs, and $CaNb_2O_6$-700 NFs, respectively. As observed in Fig. S1B, the $CaNb_2O_6$-500 NFs possesses four absorption bands. The bands around 3400 and 2450 cm^{-1} can be assigned to the surface hydroxyl group and the residual carbon-based groups (C=C=C or C=C=O) of polymer PVP, respectively.[4] Meanwhile, the band ranging from 1456 to 1635 cm^{-1} can be ascribed to the C=O, C-N, and C=C groups of residual PVP and the hydroxyl group, while the band at 500~900 cm^{-1} is originated from the stretching vibration of Nb–O bonds in the formed $CaNb_2O_6$ crystal. In comparison with the $CaNb_2O_6$-500 NFs, the stretching vibration bands belonged to the carbon-based groups of residual PVP disappear on the FT-IR spectra of both $CaNb_2O_6$-600 NFs and $CaNb_2O_6$-700 NFs. Meanwhile, the absorption bands derived from the $CaNb_2O_6$ crystal are split into three peaks with centres at 583, 753, and 875 cm^{-1}, which are attributed to the ν_3 (B_{1u}, B_{2u}, B_{3u}), ν_2 (B_{2u}), and ν_1 (B_{2u}) vibration modes of Nb–O bonds, respectively.[5-7] The above results further confirm the existence of residual carbon-based compounds in the $CaNb_2O_6$-500 NFs due to the incomplete decomposition of polymer PVP. Meanwhile, the crystallinity of the $CaNb_2O_6$-500 NFs is inferior to those of the $CaNb_2O_6$-600 NFs and $CaNb_2O_6$-700 NFs.
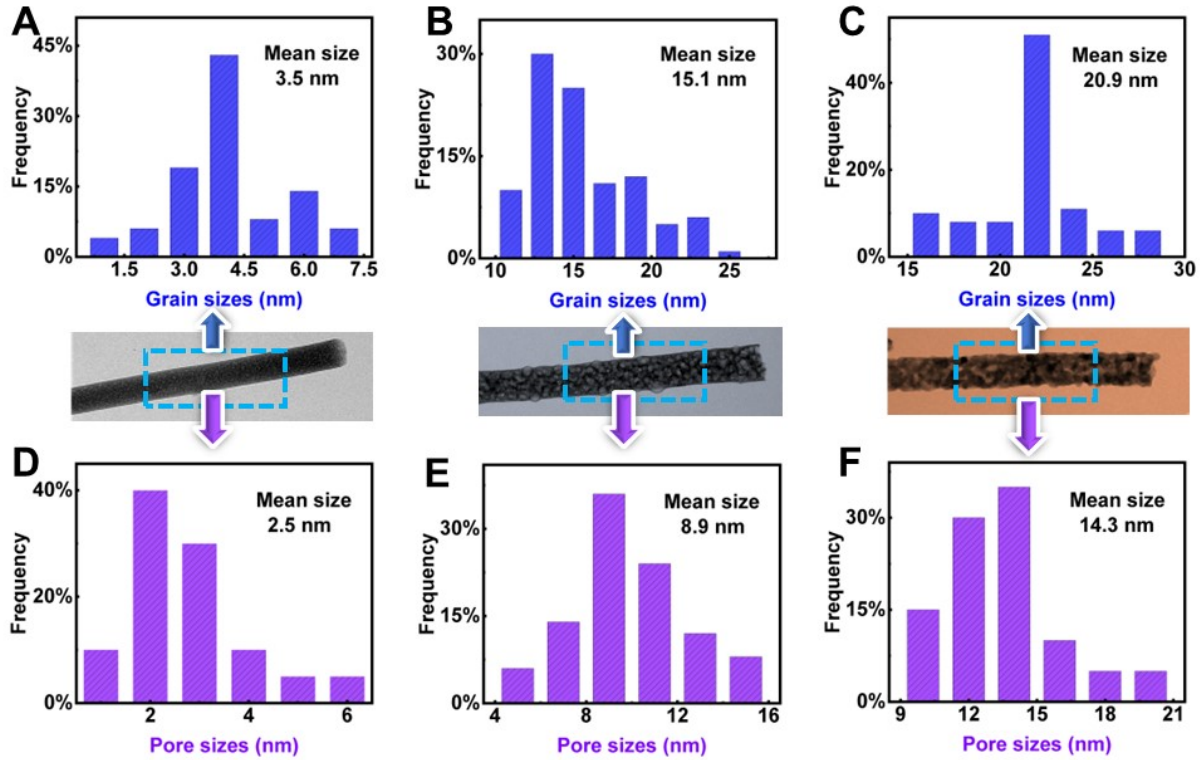
Fig. S2. Grain-size distributions of CaNb$_2$O$_6$ NPs in the (A) CaNb$_2$O$_6$-500 NFs, (B) CaNb$_2$O$_6$-600 NFs, and (C) CaNb$_2$O$_6$-700 NFs calculated from the corresponding TEM images; pore-size distributions of (D) CaNb$_2$O$_6$-500 NFs (E) CaNb$_2$O$_6$-600 NFs, and (F) CaNb$_2$O$_6$-700 NFs calculated from the corresponding TEM images.

The average grain sizes (D) of CaNb$_2$O$_6$ NPs in the electrospun NFs can be also calculated through the (041) diffraction-peak of CaNb$_2$O$_6$ by using the Debye–Scherrer formula:[8]

$$D = \frac{K \times \lambda}{B \times \cos\theta}$$

(1)

Where D is the average grain size, K is Scherrer constant (0.89), and B is the full width at half-maximum (FWHM), θ is the diffraction angle, λ is the X-ray wavelength (1.54056 A). The results indicate that the average grain-sizes of CaNb$_2$O$_6$-600 NFs and CaNb$_2$O$_6$-700 NFs were estimated to be ~16 and ~22 nm, respectively.

Furthermore, the mean sizes of CaNb$_2$O$_6$ NPs in the CaNb$_2$O$_6$-500 NFs, CaNb$_2$O$_6$-600 NFs, and CaNb$_2$O$_6$-700 NFs were ~3.5, ~15.1, and ~20.9 nm, respectively. These values are basically coincided with the values obtained from the Debye–Scherrer formula.

The mean sizes of nanopores in the CaNb$_2$O$_6$-500 NFs, CaNb$_2$O$_6$-600 NFs, and CaNb$_2$O$_6$-700 NFs were ~2.5, ~8.9, and ~14.3 nm, respectively.
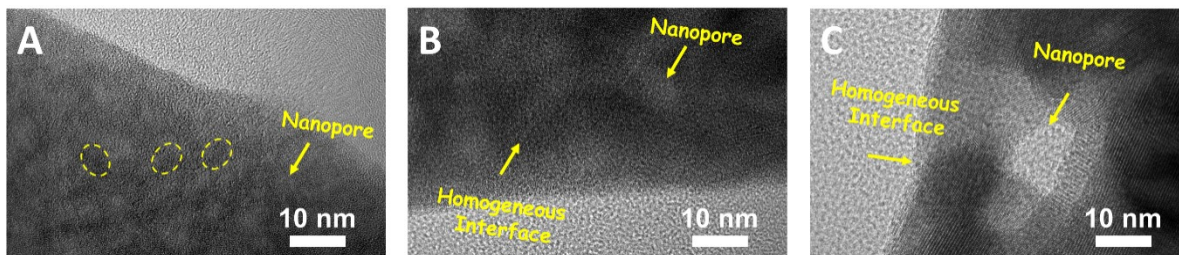
Fig. S3. HRTEM images of nanopores between the $CaNb_2O_6$ NPs in (A) $CaNb_2O_6$-500 NFs
(B) $CaNb_2O_6$-600 NFs, and (C) $CaNb_2O_6$-700 NFs.
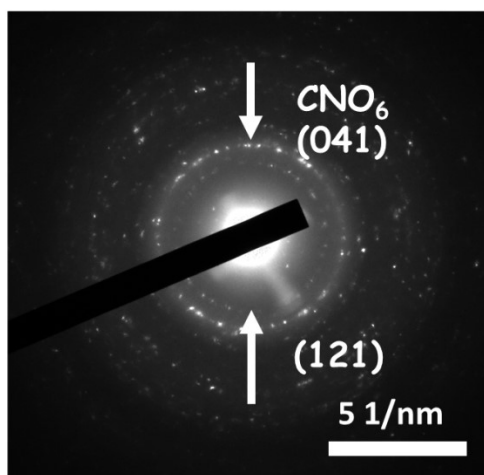

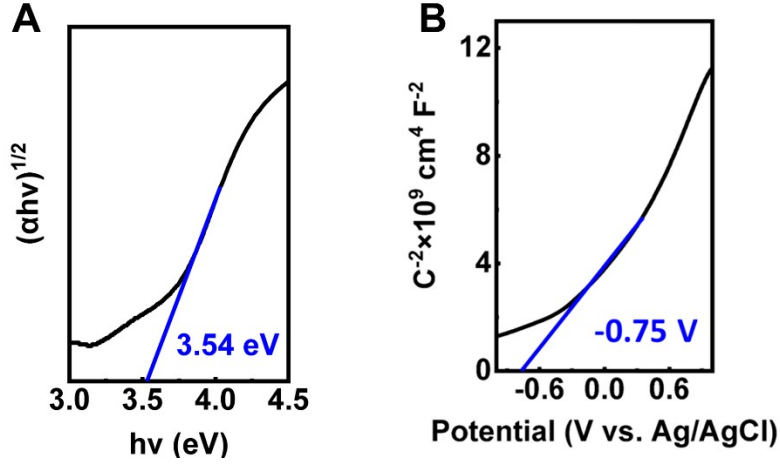**Fig. S4.** SAED pattern of the $CaNb_2O_6$-500 NFs.

Fig. S5. (A) Mott-Schottky plot and (B) plot of the $(\alpha h\nu)^{1/2}$ versus photon energy (hν) for the CaNb$_2$O$_6$-600 NFs.

The flat-band potential (E_{fb}) of the CaNb$_2$O$_6$-600 NFs can be measured through the Mott-Schottky plot based on the following formula:[9, 10]

$$\frac{1}{C^2} = \frac{2}{\varepsilon\varepsilon_0 N_D}\left(E - E_{fb} - \frac{k_B T}{q}\right)$$

(2)

Where C is the space charge capacitance; N_D, ε, and ε_0 denote the donor density, dielectric constant of the semiconductor electrode, and permittivity in vacuum, respectively; E denotes the applied potential; and q, k_B, and T represent the electronic charge, Boltzmann's constant, and absolute temperature, respectively. As observed in Fig. S7A, the (E_{fb}) value of the CaNb$_2$O$_6$-600 NFs is evaluated to be -0.75 V relative to the Ag/AgCl. The potentials obtained under the Ag/AgCl reference electrode can be converted into the normal hydrogen electrode (NHE) potentials through the following formula:[9, 10]

$$E_{fb(vs\ NHE)} = E_{fb(pH=0,vs\ Ag/Cl)} + E_{Ag\ Cl} + 0.059 \times pH$$

(3)

where $E_{AgCl} = 0.197\ V$; the pH value of the electrolyte in our work is ≈ 7.0. The E_{fb} values for the CaNb$_2$O$_6$-600 NFs can be calculated to be $\approx$-0.14 V versus NHE (pH = 0). Please note that the E_{fb} value is usually 0.3 V below the conduction band (CB) of n-type semiconductor. Thus, the CB potential of the CaNb$_2$O$_6$-600 NFs should be about -0.44 V versus NHE (pH = 0). According to the Tauc plots constructed from the UV-vis absorption spectra, the bandgap energy (E$_g$) of the CaNb$_2$O$_6$-600 NFs is 3.54 eV. Thus, its VB potential should be 3.10 V versus NHE. Based on the analyses, the energy-band configuration of the CaNb$_2$O$_6$-600 NFs is given in Fig. 2F.
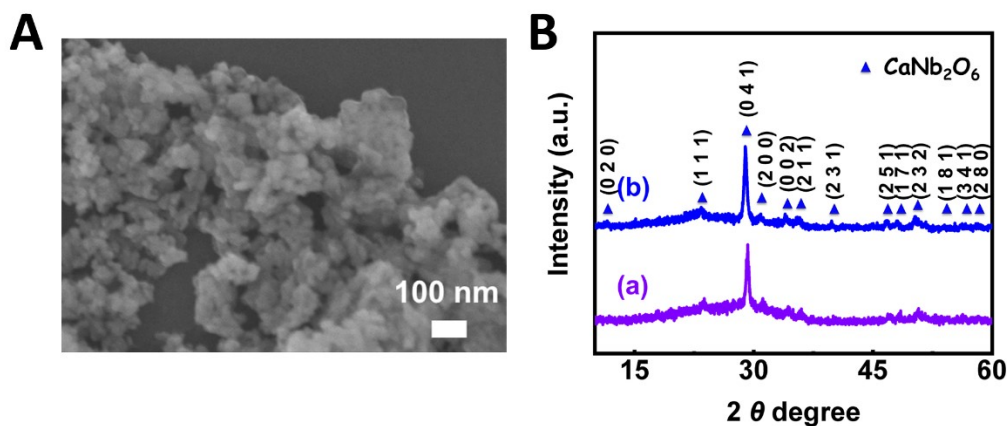
Fig. S6. (A) SEM image of the CaNb$_2$O$_6$-600 NPs; (B) XRD patterns of (a) CaNb$_2$O$_6$-600 NPs and (b) CaNb$_2$O$_6$-600 NFs.
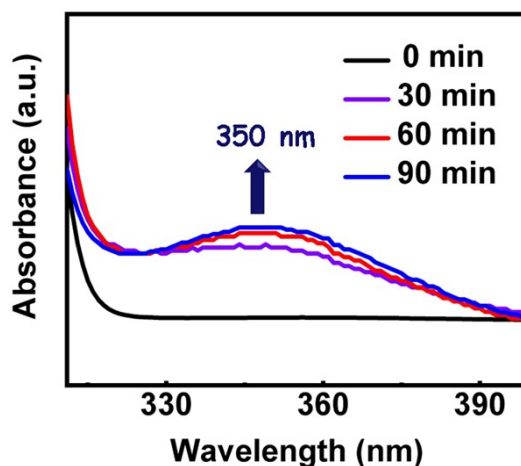

Fig. S7. UV-vis absorption spectra of the reference solution (C$_8$H$_5$KO$_4$ and KI) when adding the photocatalytic reaction solution over the CaNb$_2$O$_6$-600 NPs in dark and upon UV-visible light irradiation at different times.

To determine the oxidation product of CaNb$_2$O$_6$-600 NPs, we performed the H$_2$O$_2$ assay on CaNb$_2$O$_6$-600 NPs. As shown in Fig. S7, there is no absorption signal at ~350 nm when mixing the reference solution (C$_8$H$_5$KO$_4$ and KI) with the reaction solution of the CaNb$_2$O$_6$-600 NPs in dark. However, upon UV-visible light irradiation, the fluorescence signal with the peak at ~350 nm appeared, which suggests the formation of H$_2$O$_2$ through the photocatalytic water oxidation over the CaNb$_2$O$_6$-600 NPs. Meanwhile, with increasing irradiation time, the absorption intensity originated from the H$_2$O$_2$ product becomes stronger. It proves that the oxidation product of photocatalytic water splitting over CaNb$_2$O$_6$-600 NPs is H$_2$O$_2$.
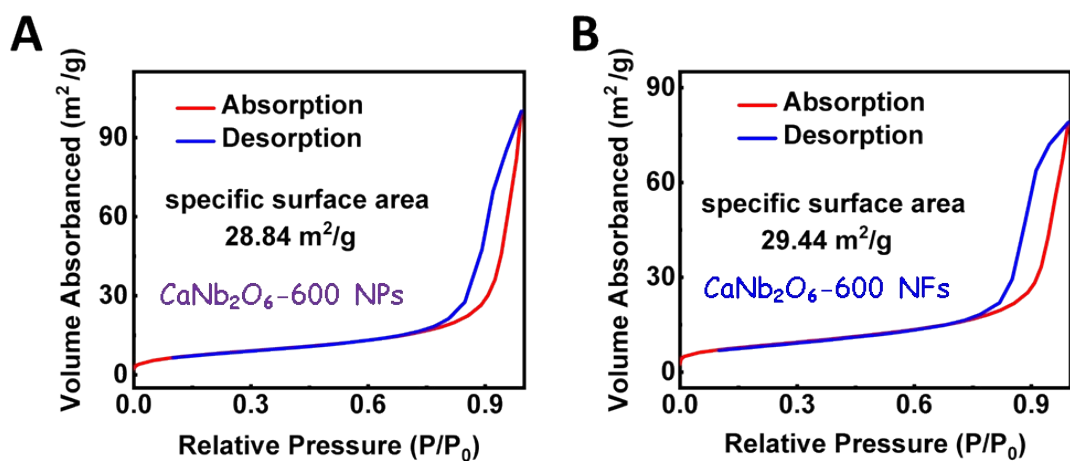
Fig. S8. Nitrogen adsorption-desorption isotherm of (A) $CaNb_2O_6$-600 NPs and (B) $CaNb_2O_6$-600 NFs.
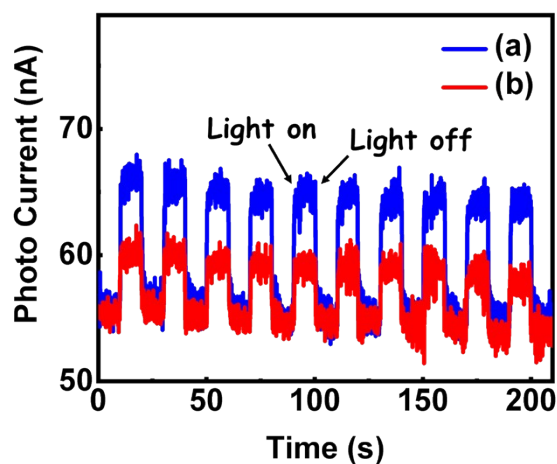

Fig. S9. Electrochemical photocurrent curves of (a) $CaNb_2O_6$-600 NFs and (b) $CaNb_2O_6$-600 NPs under UV-visible light irradiation with several on-off cycles.
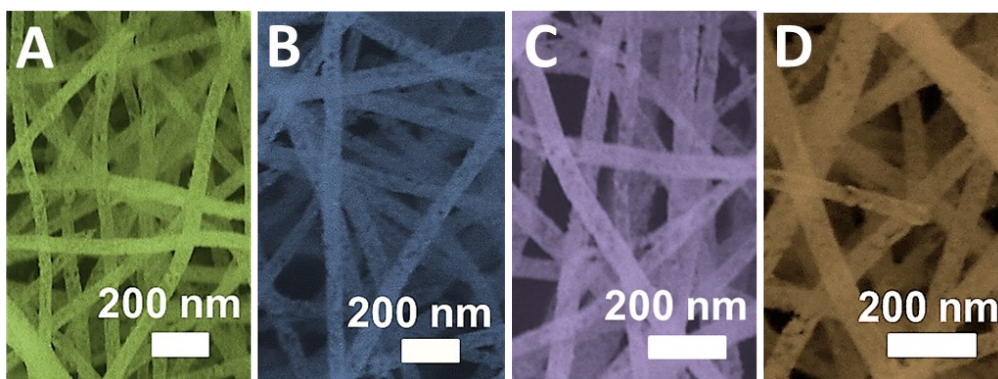

Fig. S10. SEM images of (A) $Au_{0.25}/CaNb_2O_6$, (B) $Au_{0.5}/CaNb_2O_6$, (C) $Au_{0.75}/CaNb_2O_6$, and (D) $Au_{1.25}/CaNb_2O_6$ NFs.
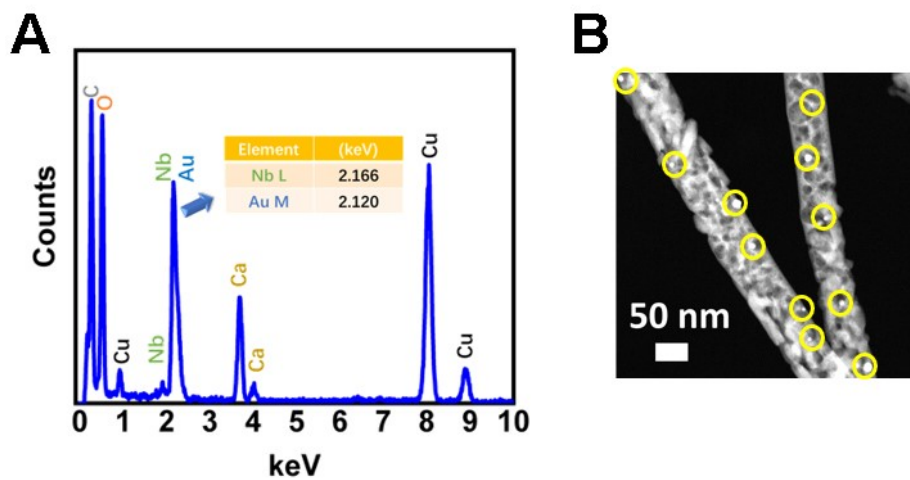
Fig. S11. (A) EDS spectra of $Au_1/CaNb_2O_6$ NFs; (B) dark-field STEM of $Au_1/CaNb_2O_6$ NFs.
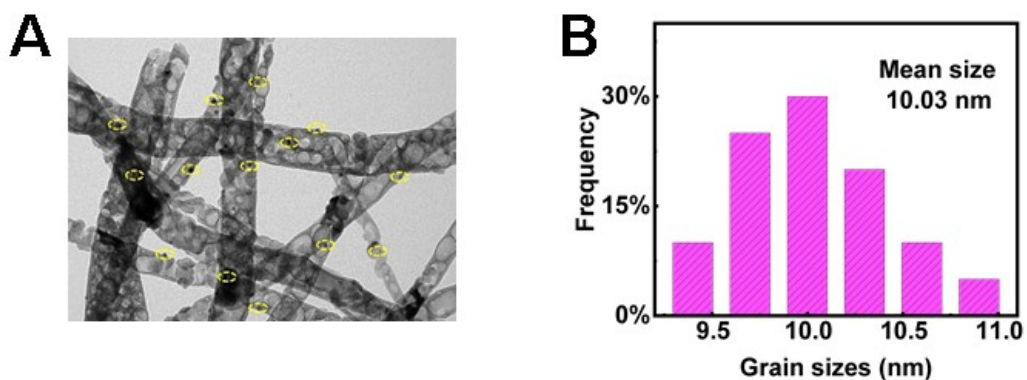

Fig. S12. (A) TEM image of $Au_1/CaNb_2O_6$ NFs and (B) the corresponding size distribution histogram of Au NPs in the NFs.
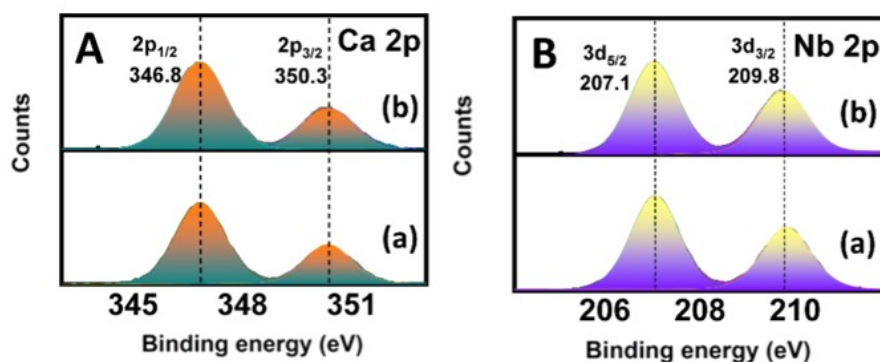
Fig. S13. XPS spectra of the as-fabricated samples: (A) Ca 2p core-level spectra; (B) Nb 2p core-level spectra: (a) $CaNb_2O_6$-600 NFs; (b) $Au_1/CaNb_2O_6$ NFs.

To determine the chemical states of the $CaNb_2O_6$-600 NFs and $Au_1/CaNb_2O_6$ NFs, the X-ray photoelectron spectroscopy (XPS) analyses were implemented. As observed in Fig. S13A, two feature peaks, corresponding to Ca $2p_{1/2}$ (346.8 eV) and Ca $2p_{3/2}$ (350.3 eV), can be detected on the Ca 2p core-level spectra of the $CaNb_2O_6$-600 NFs and $Au_1/CaNb_2O_6$ NFs. And, the spin-orbit splitting energy between the Ca $2p_{1/2}$ and Ca $2p_{3/2}$ is 3.5 eV[11], indicating the existence of Ca^{2+} state in the $CaNb_2O_6$-600 NFs and $Au_1/CaNb_2O_6$ NFs. Fig. S13B presents the Nb 2p core-level spectra of the $CaNb_2O_6$-600 NFs and $Au_1/CaNb_2O_6$ NFs, in which all the above samples display two feature peaks. The peaks centered at around 207.1 and 209.8 eV can be assigned to Nb $3d_{5/2}$ and Nb $3d_{3/2}$, respectively. And, the spin-orbit splitting energy of 2.7 eV between the Nb $3d_{5/2}$ proves the Nb^{5+} state in the $CaNb_2O_6$-600 NFs and $Au_1/CaNb_2O_6$ NFs.[12]
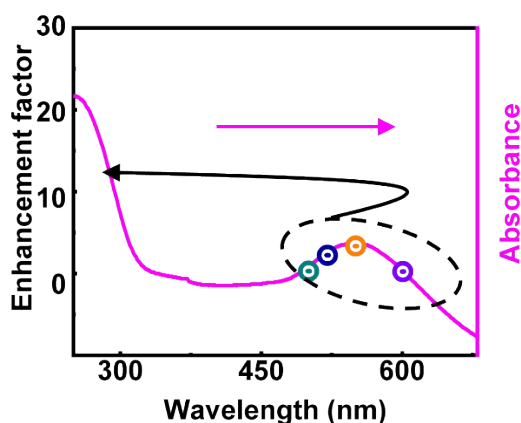

Fig. S14. UV-visible absorption spectra of the $Au_1/CaNb_2O_6$ NFs and the enhancement factor for comparing the photocatalytic H_2 production-rate of the $Au_1/CaNb_2O_6$ NFs under dual beam irradiation to the rate obtained under the single 350-nm light irradiation.
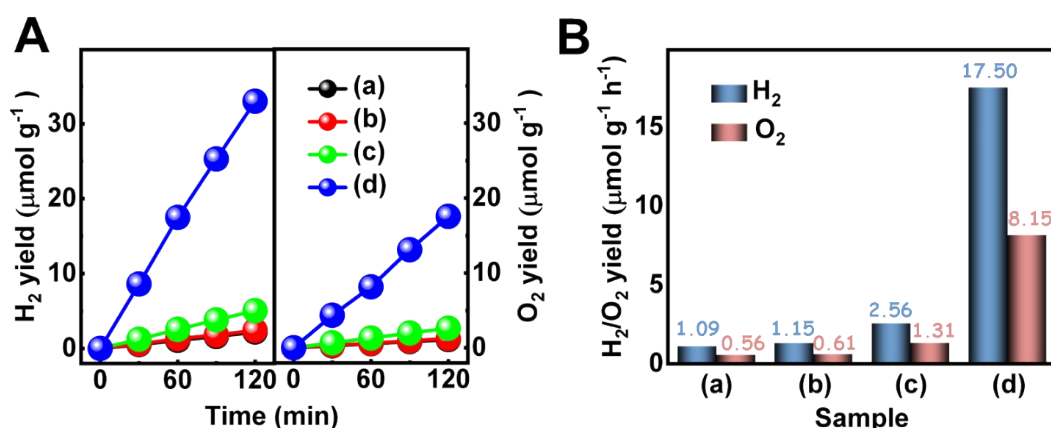
Fig. S15. (A) Photocatalytic H_2 and O_2 yields versus light irradiation time over the as-fabricated samples in pure water without adding any sacrificial agent; (B) production rates of H_2 and O_2 through the photocatalytic overall water splitting over the as-fabricated samples in pure water without adding any sacrificial agent: (a) $CaNb_2O_6$-600 NFs under single beam irradiation (350±15 nm); (b) $CaNb_2O_6$-600 NFs under dual beam irradiation (350±15 nm and >420 nm); (c) $Au_1/CaNb_2O_6$ NFs under single beam irradiation (350±15 nm); (d) $Au_1/CaNb_2O_6$ NFs under dual beam irradiation (350±15 nm and >420 nm).

To prove the hypothesis that the plasmonic Au NPs can absorb visible light to enhance the photocatalytic activity of Au NP-decorated $CaNb_2O_6$ NFs for overall water-splitting, we carried out a series of control experiments. As shown in Fig. S15, upon 350±15 nm irradiation, the production rates of H_2 (~2.56 µmol g^{-1} h^{-1}) and O_2 (~1.31 µmol g^{-1} h^{-1}) over the $Au_1/CaNb_2O_6$ NFs are about 2.3 times higher than the corresponding rates of the pure $CaNb_2O_6$ NFs (H_2: ~1.09 µmol g^{-1} h^{-1}; O_2: ~0.56 µmol g^{-1} h^{-1}). Please note that the excitation wavelength at 350±15 nm can only induce the interband transition of the $CaNb_2O_6$, but can not actuate the LSPR of Au NPs. Thus, upon 350±15 nm irradiation, the enhanced photocatalytic activity of $Au_1/CaNb_2O_6$ NFs is attributed to the "electron-sink" effect of Au NPs. In this case, Au NPs in the $Au_1/CaNb_2O_6$ NFs mainly act as the role of the cocatalyst to improve the separation of photoinduced charge-carriers.

Interestingly, when we introduced the secondary beam irradiation with the wavelength larger than 420 nm to simultaneously excite the interband transition of $CaNb_2O_6$ (350±15 nm) and the Au-LSPR (> 420 nm), the production rates of H_2 and O_2 over the $Au_1/CaNb_2O_6$ NFs could reach ~17.50 and ~8.15 µmol g^{-1} h^{-1}, respectively. These rates are ~6.8 times higher than the corresponding rates obtained from the $Au_1/CaNb_2O_6$ NFs under single irradiation at 350±15 nm. However, there was almost no obvious improvement on the photocatalytic H_2 and O_2 productions over the pure $CaNb_2O_6$ NFs under dual beam irradiation (350±15 nm and >420 nm) as compared to that under single irradiation at 350±15 nm. The above results further confirm that the plasmon-induced hot electron over Au NPs plays the leading role on the enhancement of photocatalytic activity of $Au_1/CaNb_2O_6$ NFs for water splitting. When the dual-beam irradiation (λ=350±15 nm and λ>420 nm) was introduced in the photocatalytic splitting of pure water, both the $CaNb_2O_6$ and Au LSPR in the $Au/CaNb_2O_6$ NFs were excited, the high-energy hot electrons in Au NPs could be able to rapidly transfer to the excited

CaNb$_2$O$_6$ for reduction of water into H$_2$. Meanwhile, the hot-electron transfer process could also prolong the lifetime of hot holes in Au NPs for initiating the photocatalytic water-oxidation into O$_2$. In comparison, if the single light-beam with the wavelength > 420 nm was used to only excite Au LSPR, the hot electron transfer process may be weakened due to the low conductivity of un-excited CaNb$_2$O$_6$, thus no H$_2$ and O$_2$ produced.
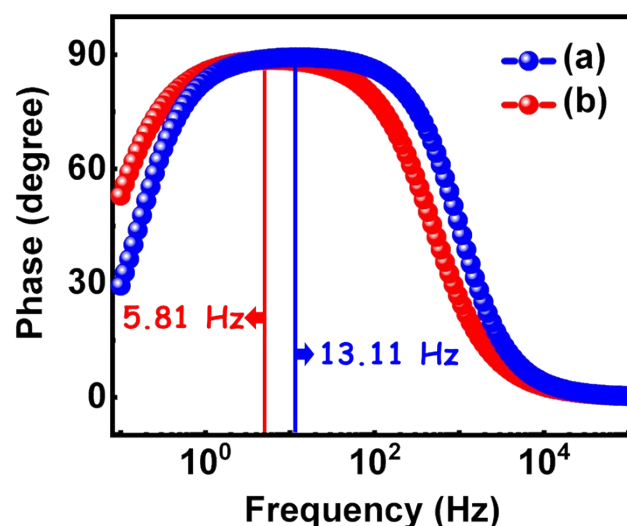

Fig. S16. Bode phase plots of Au$_1$/CaNb$_2$O$_6$ NFs measured at the open-circuit condition under (a) single beam irradiation (350±15 nm) or (b) dual beam irradiation (350±15 nm and 550±15 nm).
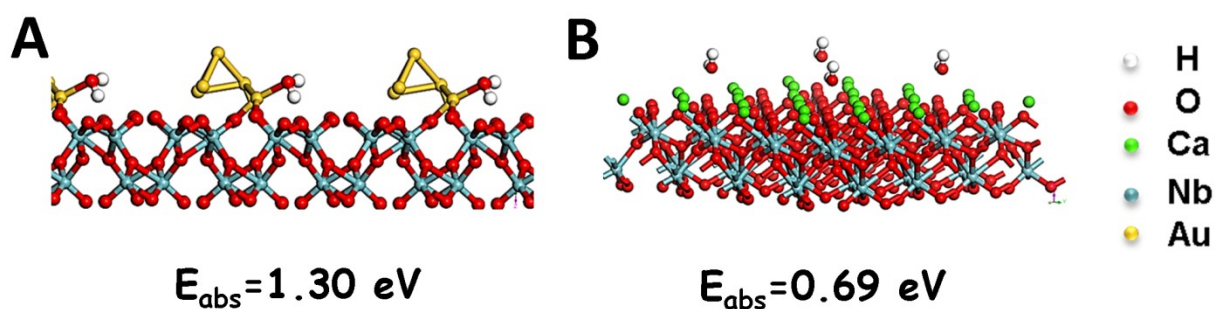

Fig. S17. Theoretical calculation results showing the chemisorption energies of H$_2$O on the different samples: (A) Au/CaNb$_2$O$_6$ interface; (B) CaNb$_2$O$_6$ surface.
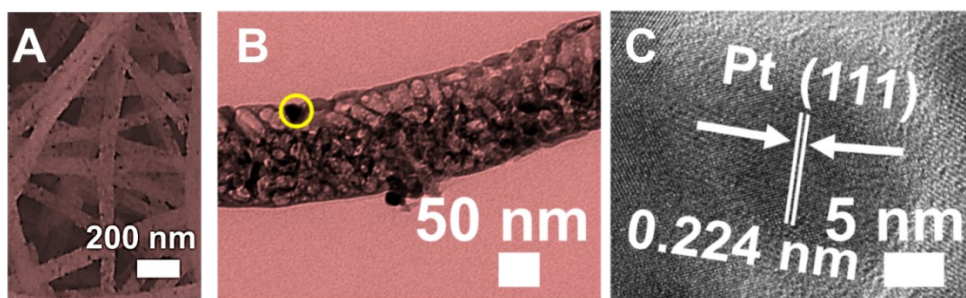
11

Fig. S18. The (A) SEM, (B) TEM image of Pt_1/ $CaNb_2O_6$ NFs, and (C) HRTEM image from the yellow-colour circle region of the image B.
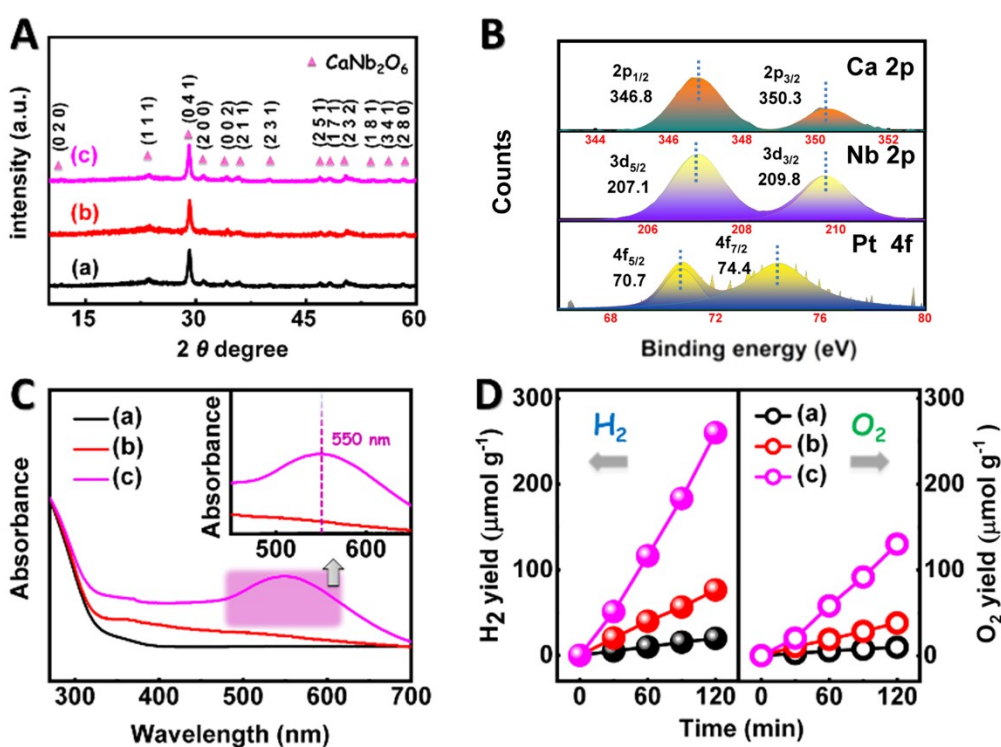

Fig. S19. (A) XRD patterns of (a) $CaNb_2O_6$-600 NFs, (b) Pt_1/$CaNb_2O_6$ NFs, (c) Au_1/$CaNb_2O_6$ NFs; (B) XPS spectra of the Pt_1/$CaNb_2O_6$ NFs: Ca 2p core-level spectrum, Nb 2p core-level spectrum, and Pt 4f core-level spectrum; (C) UV-visible absorption spectra of (a) $CaNb_2O_6$-600 NFs, (b) Pt_1/$CaNb_2O_6$ NFs, (c) Au_1/$CaNb_2O_6$ NFs; (D) plots of photocatalytic H_2 and O_2 yields versus UV-vis light irradiation time over different samples in pure water without adding any sacrificial agent: (a) $CaNb_2O_6$-600 NFs, (b) Pt_1/$CaNb_2O_6$ NFs, (c) Au_1/$CaNb_2O_6$ NFs.

As shown in Fig. S19A, all diffraction peaks on the XRD pattern of the Pt_1/$CaNb_2O_6$ NFs can also be perfectly indexed as the orthorhombic fersmite $CaNb_2O_6$ (JCPDS, no.11-619), indicating the unchanged phase structure of $CaNb_2O_6$ NFs after the introduction of Pt NPs. In addition, the characteristic diffraction peaks of Pt NPs could not be detected by using

the XRD measurement, which is due to the low content and small sizes of Pt NPs. Furthermore, the typical SEM and TEM images of the $Pt_1/CaNb_2O_6$ NF are shown in Fig. S18A and B. It can be seen that many dark spherical NPs are dispersed in the NF matrix. Fig. S18C shows the HRTEM image of spherical NPs selected from the yellow circle region of the Fig. S18B. The interplanar distance of ~0.224 nm corresponds well to the lattice spacing of Pt (111) plane. The XPS spectra indicate that the valence states of Ca and Nb ions in both the $CaNb_2O_6$ and $Pt_1/CaNb_2O_6$ NFs are +2 and +5, respectively (Fig. S19B). Meanwhile, the binding energy peaks at 70.6 and 73.9 eV are assigned to the Pt $4f_{7/2}$ and Pt $4f_{5/2}$ of metallic Pt^0.[13, 14] The above results prove the successful synthesis of the $Pt_1/CaNb_2O_6$ NFs.

Fig. S19C presents the UV-visible absorption spectra of $CaNb_2O_6$-600 NFs, $Pt_1/CaNb_2O_6$ NFs, and $Au_1/CaNb_2O_6$ NFs. Obviously, the LSPR absorption band is hardly observed on the absorption curve of the $Pt_1/CaNb_2O_6$ NFs due to the high imaginary part of the dielectric function of Pt.[15-17] The photocatalytic activity of the $Pt_1/CaNb_2O_6$ NFs for overall water-splitting was tested in comparison with those of $CaNb_2O_6$-600 NFs and $Au_1/CaNb_2O_6$ NFs under UV-visible light irradiation. As shown in Fig. S19D, the decoration of Pt NPs in the $CaNb_2O_6$ NFs only induces ~3.7-fold improvement on the photocatalytic activity for producing H_2 (~37.50 μmol g^{-1} h^{-1}) and O_2 (~19.00 μmol g^{-1} h^{-1}) as compared to that of the $CaNb_2O_6$ NFs. This improved photocatalytic activity can be attributed to the "electron sink" effect of Pt NPs. It implies that the Pt NPs can accept the photoinduced electrons of $CaNb_2O_6$ NFs across their hetero-interface, thereby suppressing the recombination process of photoinduced charge-carriers. Nevertheless, the photocatalytic activity of the $Pt_1/CaNb_2O_6$ NFs for splitting water into H_2 and O_2 was still ~3.5 times lower than those of the $Au_1/CaNb_2O_6$ NFs (H_2: ~130.02 μmol g^{-1} h^{-1}; O_2: ~66.37 μmol g^{-1} h^{-1}).
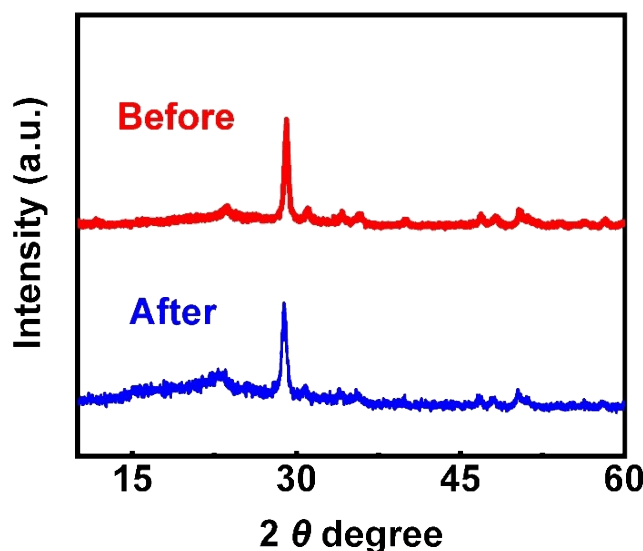

Fig. S20. XRD patterns of the $Au_1/CaNb_2O_6$ NFs before and after three cycles of photocatalytic testing.

Reference

1. Z. Zhang, X. Li, C. Wang, L. Wei, Y. Liu, C. Shao. *J.Phys. Chem. C.,* 2009, **113**, 19397-19403.

2. Y. Du, P. Yang, Z. Mou, N. Hua, L. Jiang. *Jappl. Polym. Sci.,* 2004, **99**, 23-26.

3. C. Gabriela, R. Wilson, A. Eduardo, L. Mauro, N. Jessica, T. Cecilia, M. Bruna, G. Taiana, J. Paulo, H. Luzmarina. *Mater. Chem. Phys.,* 2021, **272**, 124922.

4. C. Dudhe, S. Nagdeote, U. Palikundwar. *J. Alloy. Compd.*, 2016, **658**, 55-60.

5. D, Franklin, Hardcastle, I.Wachs. *Solid. State. Ioniss.*, 1991, **45**, 201-213.

6. R. Moreira. N, Teixeira, M.Andreeta. A.Hernandes. A. Dias. *Cryst. Growth. Des.*, 2010, **10**, 1569-1573.

7. K. Mathai, S. Vidya, Annamma John, Sam. Solomon, J. Thomsa. *Adv. Cond. Matter. Pphys.,* 2014, **6**, 645-650.

8. J. Zhu, M. Zhou, J.Xu, X. Liao. *Materials. Letters.*, 2001, **47**, 25–29.

9. S. Cao, B. Shen, T. Tong, J. Fu, J. Yu, *Adv. Funct. Mater.,* 2018, **28**, 1800136.

10. T. Tachikawa, T. Ochi, Y. Kobori, *ACS Catal.,* 2016, **6**, 2250-2256.

11. W. Yang, Z. Zhang, L. Cao, R. Ping, Q. Miao, *J. Rong. Appl. Phys. A.*, 2013, **7**, 19.

12. I.-S. Cho, S. Lee, J. H. Noh, D. W. Kim, D. K. Lee, H. S. Jung, D.-W. Kim, K. S. Hong, *J. Mater. Chem.,* 2010, **20**, 3979.

13. P. Zhang, C. Shao, X. Li, M. Zhang, X. Zhang, Y. Sun, Y. Liu, *J. Hazard. Mater.,* 2012, **237-238**, 331-338.

14. Y. Ding, Y. Wang, L. Zhang, H. Zhang, C. M. Li, Y. Lei, *Nanoscale,* 2011, **3**, 1149-1157.

15. C. Zhang, B.-Q. Chen, Z.-Y. Li, Y. Xia, Y.-G. Chen, *J. Phys. Chem. C.,* 2015, **119**, 16836-16845.

16. I. Zoric, M. Zach, B. Kasemo, C. Langhammer, *ACS Nano.,* 2011, **5**, 2535-2546.

17. Z. Zhang, A. Li, S. W. Cao, M. Bosman, S. Li, C. Xue, *Nanoscale.,* 2014, **6**, 5217-5222.